PNAS RESEARCH ARTICLE | ENGINEERING

Heterogeneous lattice strain strengthening in severely distorted crystalline solids

Jia Li[a,1], Yang Chen[a,1], Quanfeng He[b,1], Xiandong Xu[c], Hang Wang[b], Chao Jiang[a], Bin Liu[d], Qihong Fang[a,2], Yong Liu[d], Yong Yang[b,e,2], Peter K. Liaw[f], and Chain T. Liu[e]

Edited by David Weitz, Harvard University, Cambridge, MA; received January 12, 2022; accepted May 9, 2022

Multi–principal element alloys (MPEAs) exhibit outstanding mechanical properties because the core effect of severe atomic lattice distortion is distinctly different from that of traditional alloys. However, at the mesoscopic scale the underlying physics for the abundant dislocation activities responsible for strength-ductility synergy has not been uncovered. While the Eshelby mean-field approaches become insufficient to tackle yielding and plasticity in severely distorted crystalline solids, here we develop a three-dimensional discrete dislocation dynamics simulation approach by taking into account the experimentally measured lattice strain field from a model FeCoCrNiMn MPEA to explore the heterogeneous strain-induced strengthening mechanisms. Our results reveal that the heterogeneous lattice strain causes unusual dislocation behaviors (i.e., multiple kinks/jogs and bidirectional cross slips), resulting in the strengthening mechanisms that underpin the strength-ductility synergy. The outcome of our research sheds important insights into the design of strong yet ductile distorted crystalline solids, such as high-entropy alloys and high-entropy ceramics.

Multi–principal element alloys | heterogeneous lattice strain | dislocation kink/jog | strengthening mechanism | discrete dislocation dynamics

Significance

Multi–principal element alloys exhibit outstanding mechanical properties owing to severe atomic lattice distortion. However, the heterogeneous strain caused by lattice distortion at the microscopic or mesoscopic scale has been ignored for a long time because the heterogeneous strain field is difficult to quantify and characterize. Our experiments and simulations clearly show that the heterogeneous strain field can contribute to the enhanced mechanical properties of multi–principal element alloys through the new heterogeneous strain-induced strengthening mechanisms, leading to the strength-ductility synergy in severely distorted compositionally complex crystals.

The strength-ductility trade-off is a longstanding issue for conventional alloys that are usually based on one or two principal elements. In the past decade, a new alloy design strategy has been proposed to produce severely distorted crystalline solids, which are called multi–principal element alloys (MPEAs) or high-entropy alloys (HEAs) (1–4). Interestingly, the MPEAs with a simple solid-solution crystalline structure but a high degree of chemical disorder exhibit excellent mechanical properties, such as great ductility and superb strength, superior elastic strain limit, and high fatigue, fracture, corrosion, and wear resistance (5–10). These good mechanical properties of the MPEAs are believed to originate from an unusual dislocation lattice interaction, which could be associated with a heterogeneous lattice strain effect caused by the random mixing of multiple principal elements with distinct atomic sizes, bonding variations, and crystal structure differences (11–15). However, the effect of such a heterogeneous lattice strain field on the mechanisms of three-dimensional (3D) dynamic dislocation strengthening is still elusive, which can be easily shadowed by the occurrence of massive dislocation motions within a short time period and across large length scales (16–19).

On the other hand, it has been well established that discrete dislocation dynamics (DDD) simulations are capable of exploring the dynamic dislocation evolution in alloys at the mesoscopic scale (20, 21). However, one has to consider the presence of the heterogeneous lattice strain field in order to study the dynamic strain hardening in MPEAs by using DDD simulations. To the best knowledge of the authors, no attempt has yet been made to build a 3D lattice distortion model that can formally investigate the dislocation motion/multiplication/interaction, dislocation plasticity, and strain hardening at the micro or meso scale. In the present work, we first study and characterize the lattice strain field in the FeCoCrNiMn MPEA (i.e., the Cantor alloy) from experiments (22). After that, we use a random field theory to fit the heterogeneous lattice strain field to a continuum model and use the fitted result as an input for our DDD simulations (see *SI Appendix*, Text 1). Based on these results, we can then reveal the massive dynamic dislocation evolution with and without considering the heterogeneous lattice strain field. The predictions of our DDD simulations are further benchmarked with the micropillar tests of the Cantor alloy and its variants.

The lattice distortion induced heterogeneous strain distribution in the 3D space was commonly assumed to be one of the most important structural features in MPEAs. However, few previous studies have provided direct experimental evidence to support this hypothesis. To address this issue, many experimental approaches have been adopted for the direct measurement of the lattice distortion in MPEAs in recent years

Author contributions: J.L. and Q.F. designed research; J.L., Y.C., Q.H., X.X., H.W., C.J., and B.L. performed research; J.L., Y.C., Q.H., Q.F., Y.L., Y.Y., P.K.L., and C.T.L. analyzed data; and J.L., Y.C., Q.H., Q.F., and Y.Y. wrote the paper.

The authors declare no competing interest.

This article is a PNAS Direct Submission.

[1]J.L., Y.C., and Q.H. contributed equally to this work.

[2]To whom correspondence may be addressed. Email: fangqh1327@hnu.edu.cn or yonyang@cityu.edu.hk.

This article contains supporting information online at http://www.pnas.org/lookup/suppl/doi:10.1073/pnas.2200607119/-/DCSupplemental.

Published June 13, 2022.

(23). Among them, the geometric phase analysis (GPA) methods based on transmission electron microscopy (TEM) experiments have been widely used for the characterization of lattice strain in MPEAs (15, 24–26). In the present work, we adopt the GPA method to measure the atomic lattice strain of an undeformed Cantor alloy (Fig. 1*A*) in the defect-free region, as indicated by the filtered inverse fast Fourier transformation (FFT) image (Fig. 1*B*). It is evident that the normal strain along the [111] direction alternates its sign across a distance of 1–2 nm in the Cantor alloy (Fig. 1*D*), hence defying the classic Eshelby mean field theory used for traditional alloys. We calculated the root-mean-square strains within the regions of different scan size from these experimental results (*SI Appendix*, Text 1). As shown in Fig. 1*C*, the root-mean-square strains show a power law decaying relation with the scan size, which is consistent with the fractal distribution of the residual strain field reported by Shao et al. (24) and Sayles and Thomas (27). In addition, the strain distribution is relatively random, with the strain amplitude fluctuating from one atom site to another. According to the two-dimensional Weierstrass-Mandelbrot fractal method (Fig. 1*E*), we develop the 3D strain-field function described in *SI Appendix*, Text 1. The statistical results of strains (Fig. 1*F*) show that the strain-field mapping in the Cantor alloy, as acquired by the fractal function, is consistent with the experimental result. While the average strain value is close to zero, the strain distribution is wide. This trend reflects the fluctuation of the residual strain at various positions inside the crystal lattice, being consistent with the experimental statistical result (24).

The micropillar compressions were conducted to reveal the dislocation movement and multiplication in the Cantor alloy. The electron backscatter diffraction (EBSD) inverse pole figure (IPF) map shows an equiaxed grain microstructure of the Cantor alloy with an average grain size of about 80 μm (Fig. 2*A*). The grains with the [100] orientation were selected for the milling of micropillars. The microcompression stress-strain curves are presented in Fig. 2*B*. The distinct strain bursts in the stress-strain curves were associated with the event of dislocation avalanche. A representative morphology of the deformed micropillars is shown in Fig. 2*C*. The slip traces of the {111} slip planes are visible on the scanning electron microscope (SEM) image. Additionally, multiple slip systems were activated during the deformation process. The postmortem TEM characterization was conducted on the deformed micropillar to reveal the dislocation configurations. The bright-field TEM image shows a very high density of dislocations that can be keyed to the primary slip systems of $(1\bar{1}1)$and $(11\bar{1})$ planes (Fig. 2*D*), which is consistent with the calculation of the Schmid factors of all possible slipping systems along the [100] loading direction (*SI Appendix*, Table 5). To quantify the effect of the atomic lattice strain on the dislocation movement, we also performed the GPA analysis on the deformed micropillar samples. Fig. 2 *E* and *F* show the high-resolution TEM image and the corresponding inverse FFT filtered image, where the dislocations are clearly visible. Fig. 2*G* displays the corresponding atomic strain map along the [111] direction. Evidently, the lattice strains are highly localized in the regions around the dislocations, where a high lattice resistance to the dislocation movement is expected. Similar to the previous experimental findings (25), we find that the strain field around dislocations is mainly tensile in the MPEA (Fig. 2*G*). These experimental results are important and provide the crucial evidence for pursuing a more quantitative study of this phenomenon with the DDD simulations.

In order to fully understand the effect of the heterogeneous strain field on strain hardening in MPEAs, we studied several cases in our DDD simulations, including single-crystal tension, microcompression, dislocation multiplication, and cross slip. A uniaxial tension was first applied on a single crystal in the DDD simulations with and without considering local lattice distortion or, equivalently, local lattice strains (Fig. 3*A*). As expected, the lattice strain can restrict the dislocation motion, hence improving the yield strength (Fig. 3*B*). In the presence of the heterogeneous lattice strain, we find that dislocation motion at a highly distorted (or strained) site requires a great shear stress to initiate, therefore leading to dislocation multiplications at a higher stress

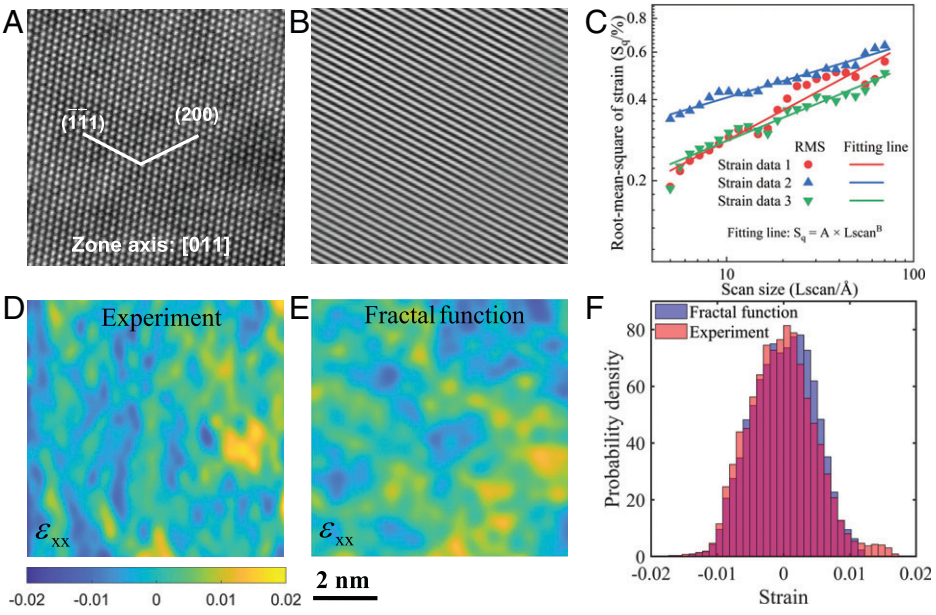

Fig. 1. Experimental characterization and characteristic analysis of a heterogeneous lattice strain field in an undeformed Cantor alloy. (*A*) The high-angle annular dark-field scanning transmission electron microscopy image with the [011] zone axis. (*B*) The filtered inverse FFT image of (111) plane of (*A*). (*C*) The correlation between the root-mean-square residual strain from the experiment and the scan size. RMS is the root-mean-square residual strain. Sq, A, B, and Lscan are the parameters of the exponential function. (*D* and *E*) The contour map of the residual strain along the [111] direction obtained by the experiment and by the fractal function, respectively. (*F*) The statistical distribution of the strain from the experiment and fractal function.

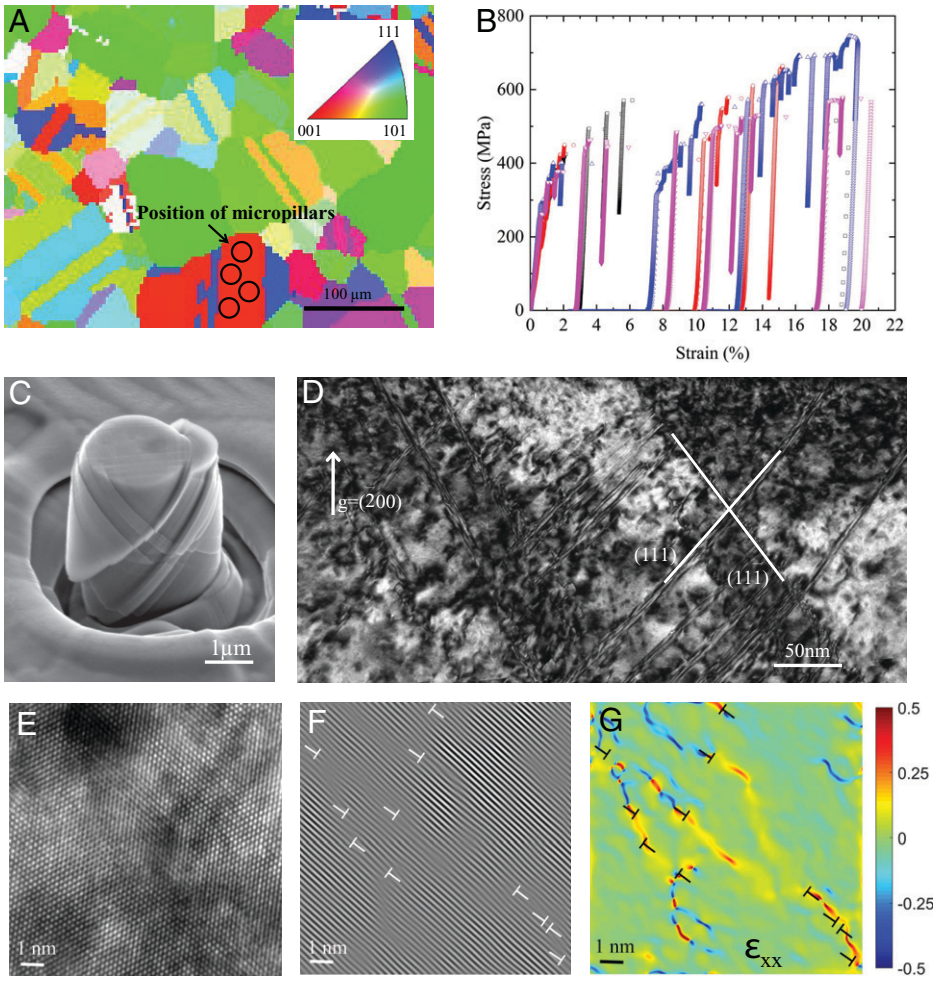

Fig. 2. Microstructures and mechanical properties of the Cantor alloy micropillar are characterized by compression experiments. (*A*) The EBSD IPF map of the Cantor alloy. The grain with the [100] direction was selected for the micropillar compression test. (*B*) The stress-strain curves of the micropillars compression along the [100] direction. The diameters of all the micropillars are 2 mm. (*C*) The SEM image shows the morphology of a deformed micropillar. (*D*) The bright-field TEM image presents slip bands in the deformed micropillar. (*E*) The high-resolution TEM image of the deformed sample with the [011] zone axis. (*F*) The filtered inverse FFT image of (111) plane of (*E*). (*G*) The corresponding atomic-scale strain map, ε_{xx}.

(Fig. 3*C*) and more slip systems being activated to further amplify dislocation multiplications at a fast rate. To reveal how the heterogeneous lattice strain influences the dislocation behavior, the evolving dislocation configurations in microcompression are shown in Fig. 3 *D*–*F*. In line with the experimental results (Fig. 2*D*), a secondary slip system is activated during the deformation process, which results in the interaction of slip traces and also cross slips that give rise to a high density of stored dislocations and a significant work hardening (Fig. 3 *D* and *E*). Here we note that the heterogeneous lattice strain can help generate a large number of mobile tortuous dislocations on multiple slip systems, leading to extensive dislocation forest strengthening. For different crystallographic orientations, the yielding strengths predicted by the current DDD simulations are consistent with the experimental measurements (Figs. 2*B* and 3*F*). Furthermore, we also discussed the relationship between the strength and heterogeneous lattice strain in a quantitative manner (see *SI Appendix*, Text 2). According to our experiments, the root-mean-square lattice strain, extrapolated from the high-resolution TEM images, can be correlated positively with the yield strengths of the MPEAs.

As one of the most important dislocation-multiplication mechanisms, Frank-Read (FR) sources play a fundamental role (28). To uncover the effect of the heterogeneous lattice strain on dislocation multiplication, the configurations of the dislocation acting as an FR source with and without lattice strains are presented in Fig. 3 *G* and *H*, respectively. Clearly, dislocation pinning is observed at the sites of high shear resistance (Fig. 3*I*). Here it is worth noting that we quantitatively assessed the effect of the heterogeneous lattice strain on the resistance against dislocation movement and derived a formula for the heterogeneous strain dependent critical resolved shear stress (*SI Appendix*, Text 2). In order to minimize the elastic energy, the configuration of a dislocation line has to vary with the local elastic stress (or strain) field (14, 15). Therefore, when a dislocation starts to move, the trajectory of its motion could be wavy and involves numerous "pinning-and-depinning" processes when the dislocation line sweeps through a fluctuating elastic stress field on the slip plane (2). This also affects the operation of the FR source, as captured by our DDD simulations (see Movies S1 and S2 for details). Within the heterogeneous lattice strain field, the dislocation slip becomes "sluggish," with multiple pinning sites being formed, which raises the dislocation density and the probability of dislocation entanglements, eventually leading to improved strain hardening. In contrast, we did not find significant strain hardening if the heterogeneous lattice strain is excluded in our DDD simulations. Recently, it was found that chemical short-range order (SRO) may be coupled with lattice distortion in altering the mechanical properties of MPEAs (25, 26, 29, 30). In such a case, we also studied the effect of SRO on the local lattice

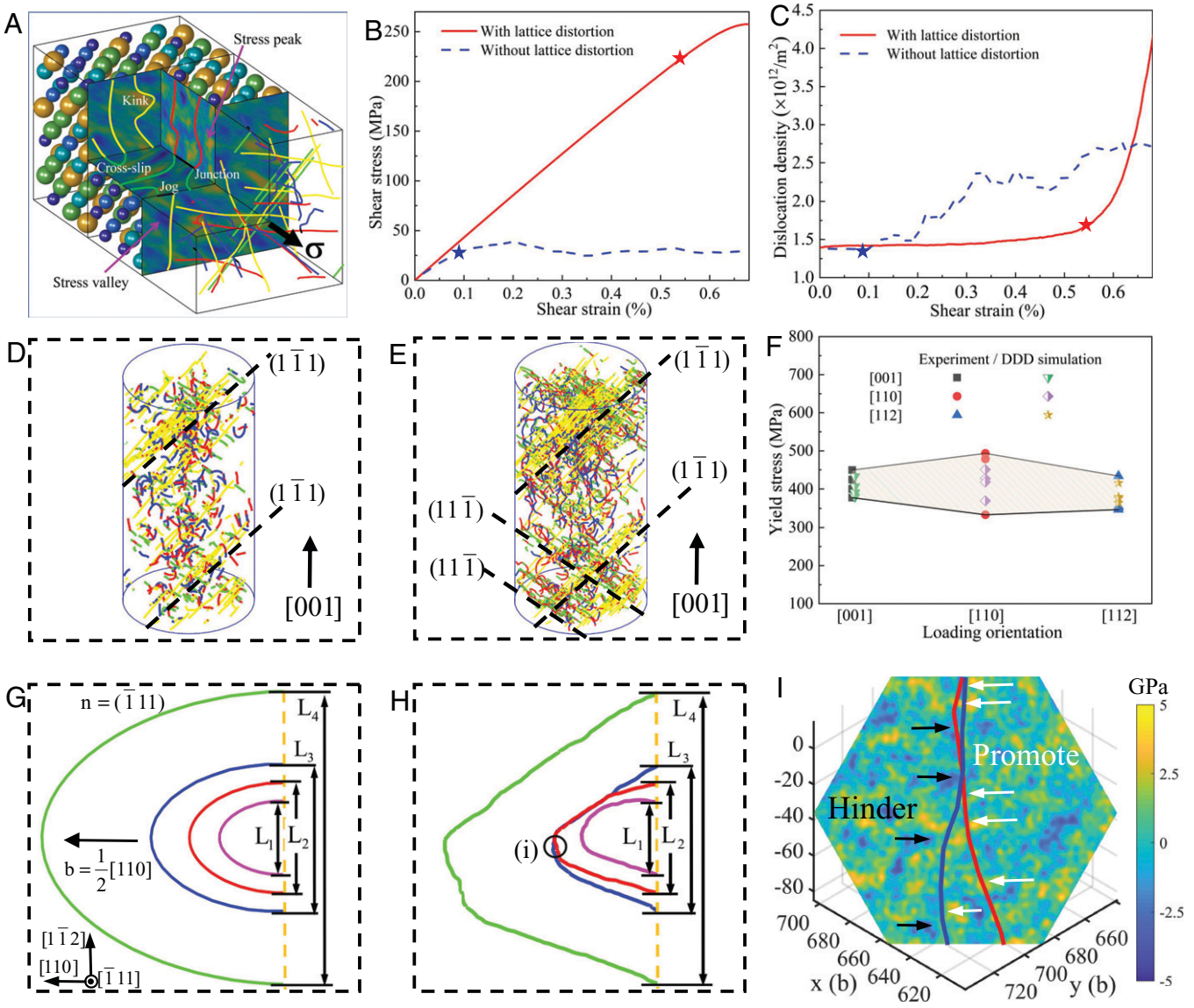

Fig. 3. Stress-strain curve and dislocation configuration/evolution in MPEAs. (*A*) Diagram of DDD simulations for MPEAs. (*B*) The relationship between the stress and strain in a bulk MPEA. (*C*) The dislocation density with increasing strain. Here, "Without lattice distortion" indicates the pure metal, which has the same elastic constant and Poisson ratio as the Cantor alloy. The five-pointed star indicates the yield point, in which the dislocation multiplication occurs. (*D* and *E*) The dislocation configurations in the micropillar at strains of 0.39 and 0.57%. The dislocations on the (111) slip plane (blue line), ($\bar{1}11$) slip plane (red line), ($1\bar{1}1$) slip plane (light yellow line), and ($11\bar{1}$) slip plane (green line). (*F*) The yielding strength of the micropillar obtained from the experiments and DDD simulations at different loading orientations. (*G* and *H*) The dislocation configurations of the FR source at the critical shear stress for different FR source lengths without and with lattice distortion, respectively. (*I*) The dislocation configuration of the FR source under the shear-stress field on the ($\bar{1}11$) dislocation slip plane along the [110] direction, where the black arrows indicate the stress valley to inhibit the dislocation motion and the white arrows indicate the stress peak to promote the dislocation motion. For (*G–I*), the pink, red, blue, and green lines indicate FR sources with source lengths of 1,000, 1,500, 2,000, and 4,000 b. Here, b is the magnitude of the Burgers vector.

strain in a model MPEA with molecular dynamics (MD) simulations (see *SI Appendix*, Text 2). Our preliminary results show that SRO may increase local shear strains; however, this is beyond the scope of the current study and will be addressed in our future work.

Aside from the FR source, we also studied the cross-slip behavior of dislocations that may involve double cross slips and multiple kinks/jogs in the presence of the heterogeneous lattice strain (Fig. 4), which can contribute to strain hardening as well. Once dislocations can be pinned at various locations in the heterogeneous lattice strain field, we observe repetitive formation and annihilation of kinks on the screw or edge dislocations when they glide on their slip plane (Fig. 4 *A* and *B*), which results in a constant change in the length of mobile dislocations (Fig. 4*C*). In theory, this dynamic behavior causes the oscillation of the elastic strain energy stored in the system, which hinders smooth dislocation movements and prompts the cross slip of dislocations (Fig. 4 *D–G*), for instance, from the ($\bar{1}11$) plane to the ($11\bar{1}$) slip plane in order to minimize local lattice resistance (*SI Appendix*, Text 3). Similarly, these dislocations can cross slip back onto the ($\bar{1}11$) plane as the plastic flow continues, resulting in a double cross slip (Fig. 4 *H*).

Interestingly, we found that the dislocation double cross slip causes not only dislocation proliferation but also the formation of dislocation walls (Movie S3). Here we note that the extensive cross slip we observed in our DDD simulations is consistent with the in situ TEM observations (15) and previous MD simulations (31), where the cross-slip rate in random face-centered cubic alloys is expected to be greatly accelerated by the reduction in local cross-slip barriers. As seen in Fig. 4 *I* and *J*, during dislocation double cross slip, our DDD simulations show that

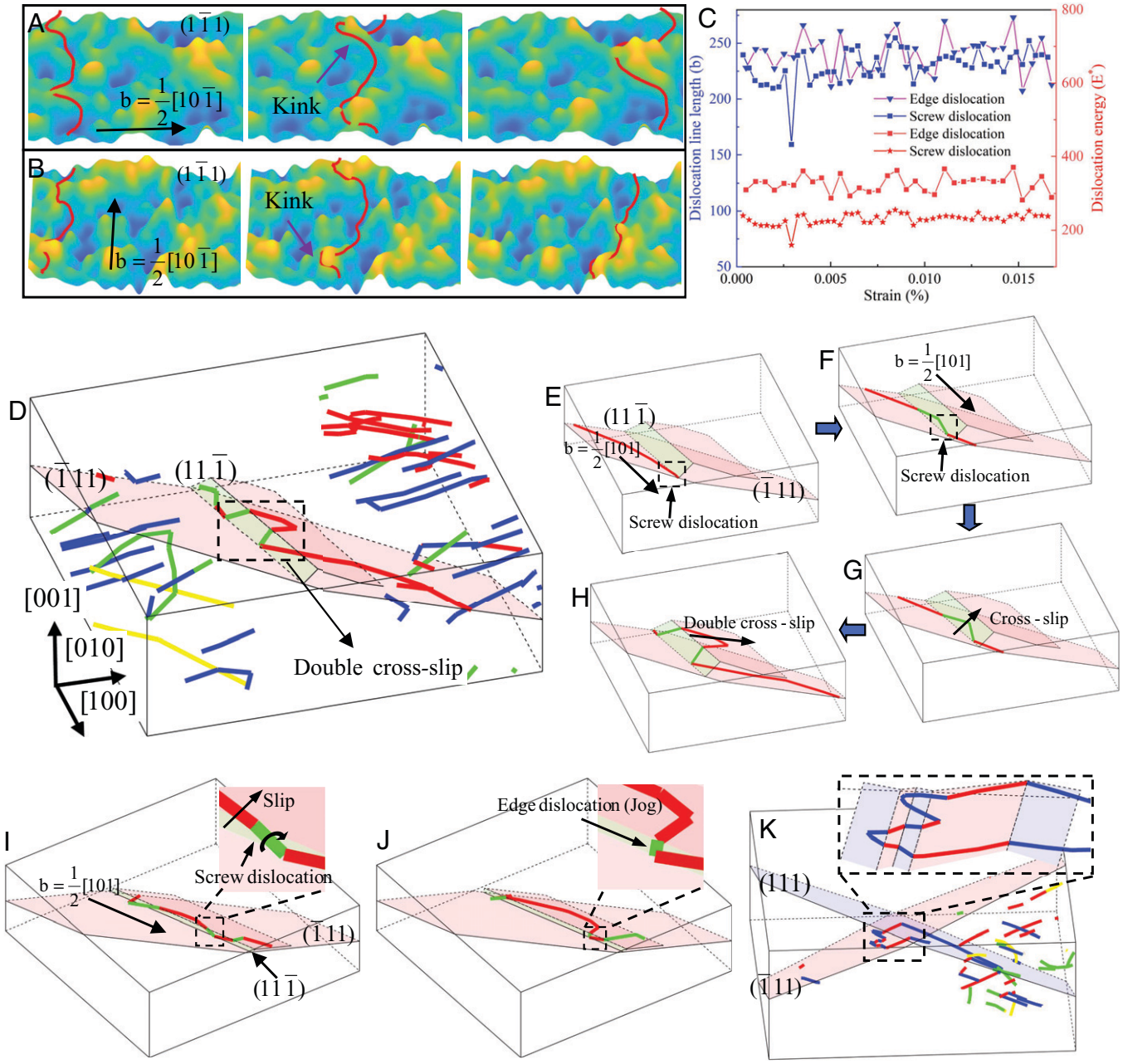

Fig. 4. Characterization of dislocation motion in MPEAs. (*A*) and (*B*) The screw/edge dislocation kink is formed at the stress peak. (*C*) The corresponding dislocation line length and energy fluctuate violently with strain (here $E^* = \mu b^2 ln(R/r_0)/4\pi$). (*D*) The dislocation evolution on the $(\bar{1}11)$ plane. (*E*–*H*) The process of cross slip and double cross slip. (*I*) Two screw dislocation segments formed on the $(11\bar{1})$ plane (green line) in the early stage of double cross slip, (*J*) then changed to two edge dislocation segments (jog) owing to the dislocation on the $(\bar{1}11)$ plane (red line), forming a bending bow under the action of the applied shear stress. (*K*) Many jogs appear on a dislocation benefiting from the multiple double cross slips.

the screw dislocation forms a jog pair on the junction of the $(11\bar{1})$ and $(\bar{1}11)$ plane (Fig. 4 *I* and *J*), which has also been observed in the early work (32). In the case of strong local pinning, we even observed the dislocation cross slip in two opposite directions (Fig. 4*K*), leading to an increased cross-slip rate and a unique multijogged dislocation configuration, which, however, was not observed in the absence of the heterogeneous lattice strain field (Movies S4 and S5).

In summary, we performed extensive experiment-informed DDD simulations to study the heterogeneous lattice strain-induced strengthening in the MPEAs in this work. In particular, we investigated single-crystal tension, micropillar compression, dislocation multiplication at FR sources, and dislocation cross slips in the presence of heterogeneous lattice strains. Our DDD simulations unravel the heterogenous strain–governed mechanisms for the strength-ductility synergy in MPEAs, which can be ascribed to a transition from conventional dislocation strengthening to heterogeneous lattice strain–boosted dislocation strengthening. In the long term, we envision that this study not only provides quantitative insights into dislocation hardening mechanisms in MPEAs but also paves the way for the development of advanced severely distorted crystalline solids by fine- or coarse-tuning the intrinsic heterogeneous lattice strains.

Experimental Methods

Materials Synthesis. The Cantor alloy samples were prepared through the arc-melting method in a high-purity argon

atmosphere. The raw materials with purities of at least 99.9 weight percent (wt.%) were remelted at least four times to ensure chemical homogeneity. The ingots were cast into a cylindrical mold with a diameter of 10 mm. Heat treatment was conducted at 1,200 °C for 30 h to obtain an equiaxed grain structure.

Characterization Methods. The sample was cut and mechanically polished with SiC papers. The EBSD characterization was conducted, with a field emission SEM (Quanta 650 FEG, FEI) at 20 kV, employing the secondary electron mode. The high-angle annular dark-field scanning TEM experiment was carried out with a FEI Titan Themis 80–300 operated at 300 kV. The high-resolution TEM experiment was carried out with a JEOL JEM 2100F microscope. The undeformed Cantor alloy TEM samples were mechanically polished to a thickness of about 50 μm. After that, the thin sheet was punched into discs with a diameter of 3 mm, followed by mechanical dimpling. Then, the TEM samples were ion milled, using Gatan PIPS Model 695, to a thickness of electron transparency. The TEM sample of the deformed micropillar was prepared on a FEI scanning electron microscope/focused ion beam (SEM/FIB) system according to the normal ion beam thinning procedure. The geometric phase analysis was carried out via the open source program Strain ++ (33).

Micropillar Compression. The micropillars were milled on an FEI SEM/FIB system. The diameter of the micropillars was about 2 μm and aspect ratio about 2. The taper angles of micropillars were all carefully controlled to be less than 2.5°. Micropillar compression tests were conducted on a Hysitron TI 950 TriboIndenter system.

Root-Mean-Square Strain. The root-mean-square value of the strain field, $\varepsilon(i,j)$, $S_q = \sqrt{\frac{1}{N_x N_y}\sum_{i=0}^{Nx-1}\sum_{j=0}^{Ny-1}\left(\varepsilon(i,j)-\bar{\varepsilon}\right)^2}$, is used to investigate the fractal characteristics of the strain field in MPEAs (27). Here, $\bar{\varepsilon}$ is the mean value, and N_x, and N_y are the numbers of samples along rows and columns on the strain image, respectively, and $N_x = 100$ and $N_y = 100$ are used in our work. The $\varepsilon(i,j)$ denotes the measured value of the strain in the pixel, (i, j), of the image.

Structure-Function Method. The strain-scale parameter, H, and the fractal dimension, D, of the strain field can be calculated by the structure-function method (34). Three-dimensional structure function is defined as $S(\tau_x,\tau_y) = \langle (z(x,y) - z(x+\tau_x, y+\tau_y))^2 \rangle$, where $\tau_x = L_{hori}\cos\theta$ and $\tau_y = L_{hori}\sin\theta$ are the spatial distances between an original image (x, y) and its delayed copy $(x+\tau_x, y+\tau_y)$, L_{hori} is the horizontal length, and $z(x,y)$ denotes the measured strain in the pixel (x, y) of the image. The $\langle\cdots\rangle$ is the mean value. $\theta = \frac{2\pi}{n}, \frac{\pi}{n}, \ldots 2\pi$ ($n = 50$ in our work) is used to build n profiles derived from the image. Any profile of the structure function obeys the approximate scaling-law behavior $S(L_{hori}) = \Lambda(L_{hori})^{2(2-Ds)}$, where $D_p = \frac{4-Ts}{2}$ is the profile fractal dimension. In the strain-scale parameter, $H = \exp\left\{\frac{\ln\Lambda + \ln\{2\Gamma(5-2D_p)sin[(2-D_p)\pi]\} - \ln\pi}{2(D_p-1)}\right\}$, $\Gamma(x)$ is the gamma function. Ts and $\ln(\Lambda)$ are the slope and intercept of a log-log plot of S vs. L_{hori}. The surface fractal dimension is $D_{SF} = \langle D_p \rangle + 1$. The strain-field-fractal dimension is $D = D_{SF} + 1$. The fractal dimension, D_{ij}, and strain amplitude, H_{ij}, for the strain components ε_{ij} of the Cantor alloy based on experimental results are listed in *SI Appendix*, Table 1.

Discrete Dislocation Dynamics Simulations. All DDD simulations performed in our work use an open source code, ParaDiS, originally developed at the Lawrence Livermore National Laboratory (20). The parameters used in ParaDiS for the DDD simulations of the Cantor alloy are listed in *SI Appendix*, Table 3. The exceptions are explained below. In the DDD simulation of a bulk MPEA, the simulation cell is a cube with a length of 5.5 μm (35) subjected to periodic boundary conditions on all six surfaces. The dislocation structure with the initial density of $\rho_0 \approx 1.4 \times 10^{12}/m^2$ is first relaxed to an equilibrium state, and then it is subjected to the constant strain rate of $\dot{\varepsilon} = 10^4/s^1$ along $[\bar{1}23]$. The shear stress, τ, and strain, γ, are related to the normal stress, σ, and strain, ε, by $\tau = S\sigma$ and $\gamma = \varepsilon/S$, where $S = 0.4667$ with a tensile direction of $[\bar{1}23]$. The Schmid factor of the Cantor alloy under the loading direction of $[\bar{1}23]$ is listed in *SI Appendix*, Table 2. In the DDD simulation of the MPEA pillar at the tensile directions of [001], [110], and [112], the initial dislocation density is $\rho_0 \approx 6.4 \times 10^{12}/m^2$, and the diameter of the pillar is 2,000 nm according to our compression experiment (Fig. 2*C*). The Young's modulus values of the FeCoCrNiMn MPEA micropillar compression experiments are listed in *SI Appendix*, Table 4, and the average of Young's modulus (about 74.5 GPa) is used in the DDD simulation of micropillar compression. The other material parameters are shown in the *SI Appendix*, Text 4.

Data Availability. All study data are included in the article and/or supporting information.

ACKNOWLEDGMENTS. The authors deeply appreciate the support from the National Natural Science Foundation of China (Grants 12172123, 12072109, and 51871092). X.X. is financially supported by the National Natural Science Foundation of China (Grant 52001120). B.L. is grateful for the financial support from the National Natural Science Foundation of China (Grant 52020105013). P.K.L. very much appreciates the support from the National Science Foundation (Grants DMR-1611180 and 1809640) and Army Research Office (Grants W911NF-13-1-0438 and W911NF-19-2-0049). The research of Y.Y. is supported by the research grant council of the Hong Kong government, through the general research fund with the Grant Numbers N_CityU 109/21, CityU11200719, and CityU11213118.

Author affiliations: [a]State Key Laboratory of Advanced Design and Manufacturing for Vehicle Body, College of Mechanical and Vehicle Engineering, Hunan University, Changsha 410082, China; [b]Department of Mechanical Engineering, College of Engineering, City University of Hong Kong, Kowloon Tong, Kowloon, Hong Kong SAR 999077, China; [c]Centre for High Resolution Electron Microscopy, College of Materials Science and Engineering, Hunan University, Changsha 410082, China; [d]State Key Laboratory of Powder Metallurgy, Central South University, Changsha 410083, China; [e]Department of Materials Science and Engineering; Mechanical Behavior Division of Shenyang National Laboratory for Materials Science, College of Engineering, City University of Hong Kong, Kowloon Tong, Kowloon, Hong Kong SAR 999077, China; and [f]Department of Materials Science and Engineering, The University of Tennessee, Knoxville, TN 37996

1. B. Gludovatz *et al.*, A fracture-resistant high-entropy alloy for cryogenic applications. *Science* **345**, 1153–1158 (2014).
2. Z. Lei *et al.*, Enhanced strength and ductility in a high-entropy alloy via ordered oxygen complexes. *Nature* **563**, 546–550 (2018).
3. J. W. Yeh *et al.*, Nanostructured high-entropy alloys with multiple principal elements: Novel alloy design concepts and outcomes. *Adv. Eng. Mater.* **6**, 299–303 (2004).
4. T. Yang *et al.*, Multicomponent intermetallic nanoparticles and superb mechanical behaviors of complex alloys. *Science* **362**, 933–937 (2018).
5. Z. Li, K. G. Pradeep, Y. Deng, D. Raabe, C. C. Tasan, Metastable high-entropy dual-phase alloys overcome the strength-ductility trade-off. *Nature* **534**, 227–230 (2016).
6. Z. Zhang *et al.*, Nanoscale origins of the damage tolerance of the high-entropy alloy CrMnFeCoNi. *Nat. Commun.* **6**, 10143 (2015).
7. P. Shi *et al.*, Hierarchical crack buffering triples ductility in eutectic herringbone high-entropy alloys. *Science* **373**, 912–918 (2021).
8. M. Zhang *et al.*, Single-layered organic photovoltaics with double cascading charge transport pathways: 18% efficiencies. *Nat. Commun.* **12**, 309 (2021).

9. Y. J. Liang *et al.*, High-content ductile coherent nanoprecipitates achieve ultrastrong high-entropy alloys. *Nat. Commun.* **9**, 4063 (2018).
10. Q. F. He *et al.*, A highly distorted ultraelastic chemically complex Elinvar alloy. *Nature* **602**, 251–257 (2022).
11. S. S. Sohn *et al.*, Ultrastrong medium-entropy single-phase alloys designed via severe lattice distortion. *Adv. Mater.* **31**, e1807142 (2019).
12. Y. Zou, H. Ma, R. Spolenak, Ultrastrong ductile and stable high-entropy alloys at small scales. *Nat. Commun.* **6**, 7748 (2015).
13. F. Wang *et al.*, Multiplicity of dislocation pathways in a refractory multiprincipal element alloy. *Science* **370**, 95–101 (2020).
14. Q. J. Li, H. Sheng, E. Ma, Strengthening in multi-principal element alloys with local-chemical-order roughened dislocation pathways. *Nat. Commun.* **10**, 3563 (2019).
15. Q. Ding *et al.*, Tuning element distribution, structure and properties by composition in high-entropy alloys. *Nature* **574**, 223–227 (2019).
16. S. Chen *et al.*, Real-time observations of TRIP-induced ultrahigh strain hardening in a dual-phase CrMnFeCoNi high-entropy alloy. *Nat. Commun.* **11**, 826 (2020).
17. S. Lee *et al.*, In-situ observation of the initiation of plasticity by nucleation of prismatic dislocation loops. *Nat. Commun.* **11**, 2367 (2020).
18. L. Zou *et al.*, Dislocation nucleation facilitated by atomic segregation. *Nat. Mater.* **17**, 56–63 (2018).
19. S. Huang *et al.*, Twinning in metastable high-entropy alloys. *Nat. Commun.* **9**, 2381 (2018).
20. V. V. Bulatov *et al.*, Dislocation multi-junctions and strain hardening. *Nature* **440**, 1174–1178 (2006).
21. R. B. Sills, N. Bertin, A. Aghaei, W. Cai, Dislocation networks and the microstructural origin of strain hardening. *Phys. Rev. Lett.* **121**, 085501 (2018).
22. B. Cantor, I. T. H. Chang, P. Knight, A. J. B. Vincent, Microstructural development in equiatomic multicomponent alloys. *Mater. Sci. Eng. A* **375**, 213–218 (2004).
23. L. R. Owen, N. G. Jones, Lattice distortions in high-entropy alloys. *J. Mater. Res.* **33**, 2954–2969 (2018).
24. Y. T. Shao, R. Yuan, Y. Hu, Q. Yang, J. M. Zuo, The paracrystalline nature of lattice distortion in a high entropy alloy. arXiv [Preprint] (2019). https://doi.org/10.48550/arXiv.1903.04082 (Accessed 7 June 2022).
25. X. Chen *et al.*, Direct observation of chemical short-range order in a medium-entropy alloy. *Nature* **592**, 712–716 (2021).
26. R. Zhang *et al.*, Short-range order and its impact on the CrCoNi medium-entropy alloy. *Nature* **581**, 283–287 (2020).
27. R. S. Sayles, T. R. Thomas, Surface topography as a nonstationary random process. *Nature* **271**, 431–434 (1978).
28. J. Krebs *et al.*, Cast aluminium single crystals cross the threshold from bulk to size-dependent stochastic plasticity. *Nat. Mater.* **16**, 730–736 (2017).
29. S. Chen *et al.*, Simultaneously enhancing the ultimate strength and ductility of high-entropy alloys via short-range ordering. *Nat. Commun.* **12**, 4953 (2021).
30. Q. F. He *et al.*, Understanding chemical short-range ordering/demixing coupled with lattice distortion in solid solution high entropy alloys. *Acta Mater.* **216**, 117140 (2021).
31. W. G. Nöhring, W. A. Curtin, Design using randomness: A new dimension for metallurgy. *Scr. Mater.* **187**, 210–215 (2020).
32. W. Sun *et al.*, Precipitation strengthening of aluminum alloys by room-temperature cyclic plasticity. *Science* **363**, 972–975 (2019).
33. M. J. Hÿtch, E. Snoeck, R. Kilaas, Quantitative measurement of displacement and strain fields from HREM micrographs. *Ultramicroscopy* **74**, 131–146 (1998).
34. J. J. Wu, Analyses and simulation of anisotropic fractal surfaces. *Chaos Solitons Fractals* **13**, 1791–1806 (2002).
35. N. L. Okamoto *et al.*, Size effect, critical resolved shear stress, stacking fault energy, and solid solution strengthening in the CrMnFeCoNi high-entropy alloy. *Sci. Rep.* **6**, 35863 (2016).